

RESEARCH ARTICLE

10.1002/2017JC012711

Mechanism of seasonal eddy kinetic energy variability in the eastern equatorial Pacific Ocean

Minyang Wang^{1,2}, Yan Du^{1,2} , Bo Qiu³ , Xuhua Cheng¹ , Yiyong Luo⁴, Xiao Chen⁵ , and Ming Feng⁶ 

Key Points:

- EKE in the eastern equatorial Pacific Ocean exhibits a significant seasonal cycle and peaks in boreal fall season
- EKE variability attributes to the seasonal thermocline trough along 4°N, which strengthens the barotropic-baroclinic instability
- The change of the thermocline trough is further identified to be forced by the seasonal-dependent southerly winds

Correspondence to:

Y. Du,
duyan@sco.io.ac.cn

Citation:

Wang, M., Y. Du, B. Qiu, X. Cheng, Y. Luo, X. Chen, and M. Feng (2017), Mechanism of seasonal eddy kinetic energy variability in the eastern equatorial Pacific Ocean, *J. Geophys. Res. Oceans*, 122, doi:10.1002/2017JC012711.

Received 18 JAN 2017

Accepted 25 MAR 2017

Accepted article online 31 MAR 2017

¹State Key Laboratory of Tropical Oceanography, South China Sea Institute of Oceanology, Chinese Academy of Sciences, Guangzhou, China, ²University of Chinese Academy of Sciences, Beijing, China, ³Department of Oceanography, University of Hawaii at Manoa, Honolulu, Hawaii, USA, ⁴Ocean University of China, Qingdao, China, ⁵College of Oceanography, Hohai University, Nanjing, China, ⁶CSIRO Oceans and Atmosphere, Crawley, Western Australia, Australia

Abstract Enhanced mesoscale eddy activities or tropical instability waves (TIWs) exist along the northern front of the cold tongue in the eastern equatorial Pacific Ocean. In this study, we investigate seasonal variability of eddy kinetic energy (EKE) over this region and its associated dynamic mechanism using a global, eddy-resolving ocean general circulation model (OGCM) simulation, the equatorial mooring data, and satellite altimeter observations. The seasonal-varying enhanced EKE signals are found to expand westward from 100°W in June to 180°W in December between 0°N and 6°N. This westward expansion in EKE is closely connected to the barotropically-baroclinically unstable zonal flows that are in thermal-wind balance with the seasonal-varying thermocline trough along 4°N. By adopting an 1½-layer reduced-gravity model, we confirm that the seasonal perturbation of the thermocline trough is dominated by the anticyclonic wind stress curl forcing, which develops due to southerly winds along 4°N from June to December.

Plain Language Summary The sea surface temperature (SST) in the eastern equatorial Pacific Ocean exhibits a cusp-like pattern called tropical instability waves (TIWs) with wavelengths on the orders of 1000 km. They could impact the marine primary production and the cloud formation. They were previously proved to be caused by the shear of ocean currents. In this study, we found it is the tightened ocean temperature structure to reinforce the currents. And this tightened structure is forced by the seasonal-dependent southerly winds from June to December.

1. Introduction

Energetic, mesoscale perturbations of ocean currents and temperature exist in the central and eastern equatorial Pacific Ocean during the boreal summer, autumn, and winter. First documented by *Duing et al.* [1975] and *Legeckis* [1977], the perturbations often appear to be wavelike, with periods and wavelengths on the orders of 10 days and 1000 km, respectively. The perturbations in the sea surface temperature (SST) fronts of equatorial cold tongue are interpreted as tropical instability waves (TIWs, Figure 1), which are a train of westward propagating eddies called tropical instability vortices [*Flament et al.*, 1996]. The TIWs-induced oceanic eddy heat flux toward the equator has been shown to be comparable to the Ekman heat flux away from the equator and the large-scale net air-sea heat flux over the eastern tropical Pacific Ocean [*Hansen and Paul*, 1984; *Bryden and Brady*, 1989; *Baturin and Niiler*, 1997; *Swenson and Hansen*, 1999; *Wang and McPhaden*, 1999; *Jochum and Murtugudde*, 2006]. TIWs play an important role in the large-scale energy and heat balance of the equatorial cold tongue.

Energy sources for eddy kinetic energy (EKE) in the TIWs area were demonstrated to be barotropic and baroclinic instabilities in early observational and numerical studies of the TIWs energy budget [*Philander*, 1978; *Cox*, 1980; *Weisberg*, 1984; *Luther and Johnson*, 1990]. The barotropic instability was attributed to intense velocity shears between the Equatorial Undercurrent (EUC) and the South Equatorial Current (SEC) north of the equator [*Philander*, 1976; *Qiao and Weisberg*, 1995] and between the SEC and the North Equatorial Countercurrent (NECC) [*Philander*, 1978; *Flament et al.*, 1996]. Kinetic energy is converted from the mean flows to eddy flows by the barotropic instability of the horizontal circulation. In terms of the baroclinic instability,

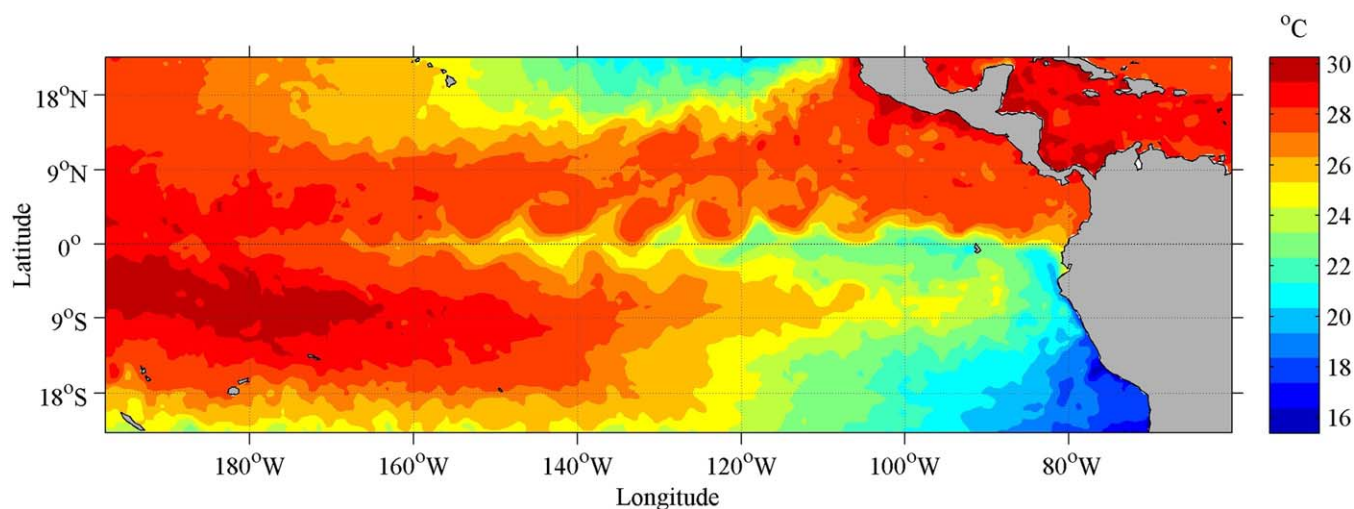


Figure 1. Daily SST map in the central and eastern tropical Pacific on 25 June 2010 based on the OISST (Optimum Interpolation Sea Surface Temperature, downloaded from the website of <http://www.ncdc.noaa.gov/oisst>). The cusp-shaped wave patterns along the equatorial SST fronts near $\sim 3^\circ\text{N}$ are due to the TIWs.

significant conversion from eddy potential energy (EPE) to EKE takes place as well in a multilevel numerical model when the waves reach larger amplitude [Cox, 1980]. The baroclinic point was validated by direct observations that cold water subducts beneath warmer water and move northward beyond 3°N across a narrow front at 2.1°N , 140°W [Johnson, 1996]. The EPE is converted into EKE by the subduction of relatively dense water, which then may be incorporated into larger instability waves. Further evidence had been shown by following studies [Masina *et al.*, 1999; Marchesiello *et al.*, 2011], and it was turned out that the baroclinic instability plays a role during the development phase of the waves.

Early satellite and in situ observations showed that the TIWs develop in the boreal summer and peak in the autumn and winter. Seasonal-varying sources for the EKE were estimated to be primarily the barotropic conversion from mean kinetic energy (MKE) in the boreal summer and autumn, and the baroclinic conversion from EPE in the boreal winter using in situ observations during the Hawaii-to-Tahiti Shuttle Experiment in 1979–1980 [Luther and Johnson, 1990] and the Tropical Instability Wave Experiment in 1990–1991 [Qiao and Weisberg, 1998]. Due to the lack of fine-scale observations, however, little attention has been paid to the seasonal cycle of the EKE, and impact of the thermocline and trade winds upon the seasonal variability of the EKE in the central and eastern equatorial Pacific Ocean remains unclear.

Improvements in eddy-resolved ocean general circulation model (OGCM) and observations make it now possible to offer high-resolution data sets to explore this problem. Previous studies [Kessler, 2006] have shown that there are two zonal thermocline ridges and one trough that form the alternatively directing surface zonal flows in the eastern equatorial Pacific Ocean within 10°S – 15°N . We hypothesize that the barotropic and baroclinic instabilities are related to this spatial patterns of the thermocline. As the trade winds vary with the season, the thermocline ridge and trough change accordingly, which in turn modify the stability properties of the regional ocean circulation and potentially affect the generation of eddies in the TIWs area. A discussion of this dynamic mechanism associated with the seasonal changes in the thermocline and trade winds will be the main purpose of this study.

The paper is organized as follows. Section 2 describes the output of a global eddy-resolving OGCM simulation and makes comparisons with available observations. Section 3 discusses the dynamic mechanism of the seasonal variability of the EKE. Discussion and summary are presented in sections 4 and 5, respectively.

2. Data and Method

2.1. Model Data

Model data from an eddy-resolving OGCM for the Earth Simulator (OFES) is used as it captures the large-scale circulation patterns and has a good representation of mesoscale eddies in the equatorial Pacific [Masumoto *et al.*, 2004; Sasaki *et al.*, 2004, 2008]. The model is based on the Modular Ocean Model version 3

(MOM3) [Pacanowski and Griffies, 2000]. The horizontal resolution is 0.1° and the number of vertical levels is 54. There are three OFES simulations (Climatological, NCEP-run, and QSCAT-run) and the QSCAT-run simulation is used in this study. The QSCAT-run simulation is initialized with the NCEP-run simulation output on 20 July 1999 and is forced subsequently by the QSCAT winds from 20 July 1999 to 30 October 2009. Output of the QSCAT-run simulation used is the 3 day snapshot of sea level anomaly (SLA), zonal/meridional/vertical velocity, potential temperature, salinity, and surface wind stress in the central and eastern equatorial Pacific Ocean from 1 January 2000 to 31 December 2008.

2.2. Evaluation of the OFES QSCAT-run

A comparison is made with the EKE derived from the observations to examine the performance of the OFES QSCAT-run in simulating EKE in the central and eastern equatorial Pacific Ocean. Following Qiu [1999], EKE in the off-equatorial open ocean can be calculated from the SLA $h(x, y, t)$ distributed by AVISO (Archiving Validation and Interpretation of Satellite Data in Oceanography).

$$EKE = \frac{1}{2} (u'^2 + v'^2), \tag{1}$$

$$u' = u - U, \quad v' = v - V \tag{2}$$

$$u = -\frac{g}{f} \frac{\partial h}{\partial y}, \quad v = \frac{g}{f} \frac{\partial h}{\partial x} \tag{3}$$

As in equation (1) the EKE is derived from 60 days (the TIWs scale) [Qiao and Weisberg, 1995, 1998] high-pass filtered velocity anomalies u', v' which are calculated by eliminating 60 days running mean U, V from u, v as in equation (2). u and v are calculated by the geostrophic flows. As in equation (3), the gravity constant $g = 9.8 \text{ m} \cdot \text{s}^{-2}$, the Coriolis parameter $f = 2\omega \sin(\phi)$ which is dependent on the latitude ϕ , and the angular rate of earth rotation $\omega = \frac{2\pi}{1\text{day}}$. The OFES SLA data are interpolated into the same horizontal grid and time interval to match the AVISO product which has a $1/3^\circ \times 1/3^\circ$ spatial resolution and a weekly time interval. For the spatial distribution of annual mean EKE (Figure 2), the AVISO product and the OFES show similar spatial patterns. The sharply elevated EKE signal is located in the box bounded by 3°N – 6°N , 180°W – 100°W with a magnitude exceeding $400 \text{ cm}^2 \cdot \text{s}^{-2}$. Averaged in the box, the surface geostrophic kinetic energy spectrum of the OFES shows very similar features to that of the AVISO product. In addition to the spectral peaks at the annual and semiannual periods, significant intraseasonal variability exists around the 33 days band corresponding to the TIWs period (Figure 3). Averaged in the box, the temporal variations of EKE derived from the OFES and AVISO exhibit highly similar seasonal and interannual variations. The linear

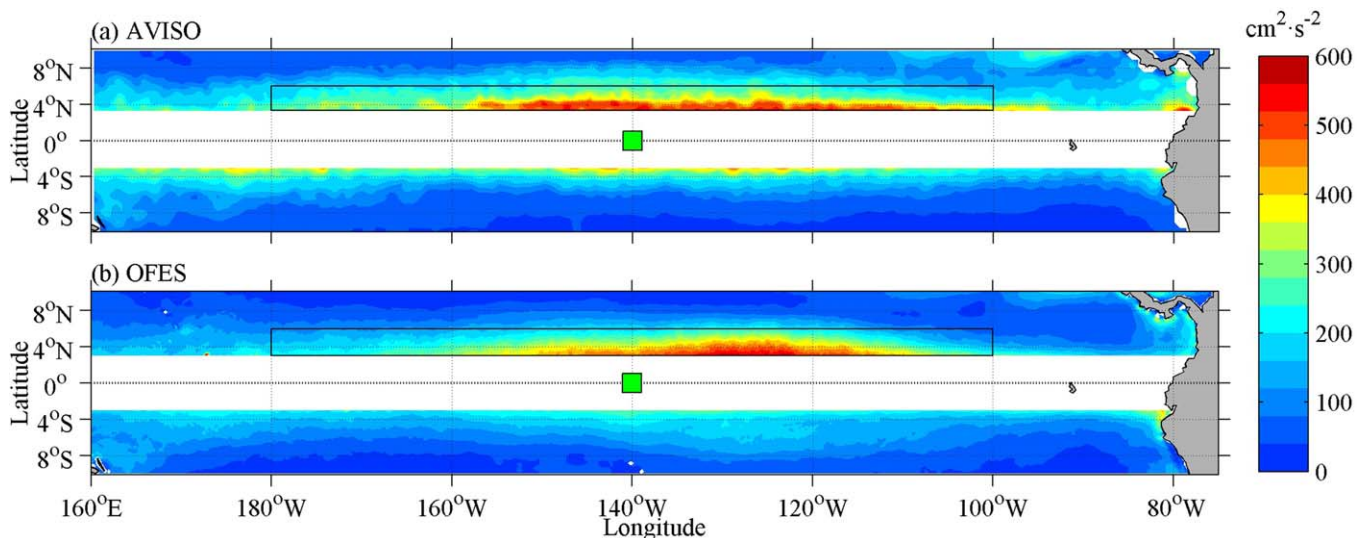


Figure 2. Annual mean EKE calculated from the SLA data of (a) AVISO and (b) OFES averaged in the year 2000–2008. The black box (3°N – 6°N , 180°W – 100°W) represents the region of elevated EKE values related to the TIWs. The green square represents one site of the TAO Array at 0°N , 140°W .

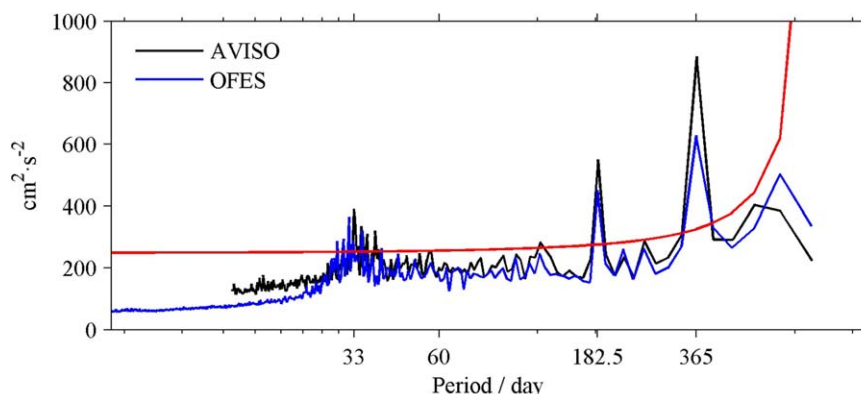


Figure 3. Kinetic energy spectrum of surface geostrophic flows calculated from the SLA data of AVISO (black line) and OFES (blue line) averaged in the black box of Figure 2. The red line represents the 95% confidence level based on the Student's *t* test.

correlation coefficient between them reaches 0.69 and is above the Student's *t* test 95% confidence level (Figure 4a).

As geostrophy does not hold near the equator due to the diminishing Coriolis parameter *f*, velocity data from the Tropical Atmosphere Ocean (TAO) Array [Hayes *et al.*, 1991] at 0°N, 140°W is used to compare with the OFES output on the equator. The daily velocity data of TAO are continuously available at the depth of 35–100 m from 1 January 2000 to 31 December 2005 and is interpolated into the same resolution of the OFES. Similar to equation (2), EKE is calculated from the 60 days high-pass filtered horizontal velocity data. Averaged from 35 to 100 m, the temporal variations of EKE derived from the OFES and TAO show similar

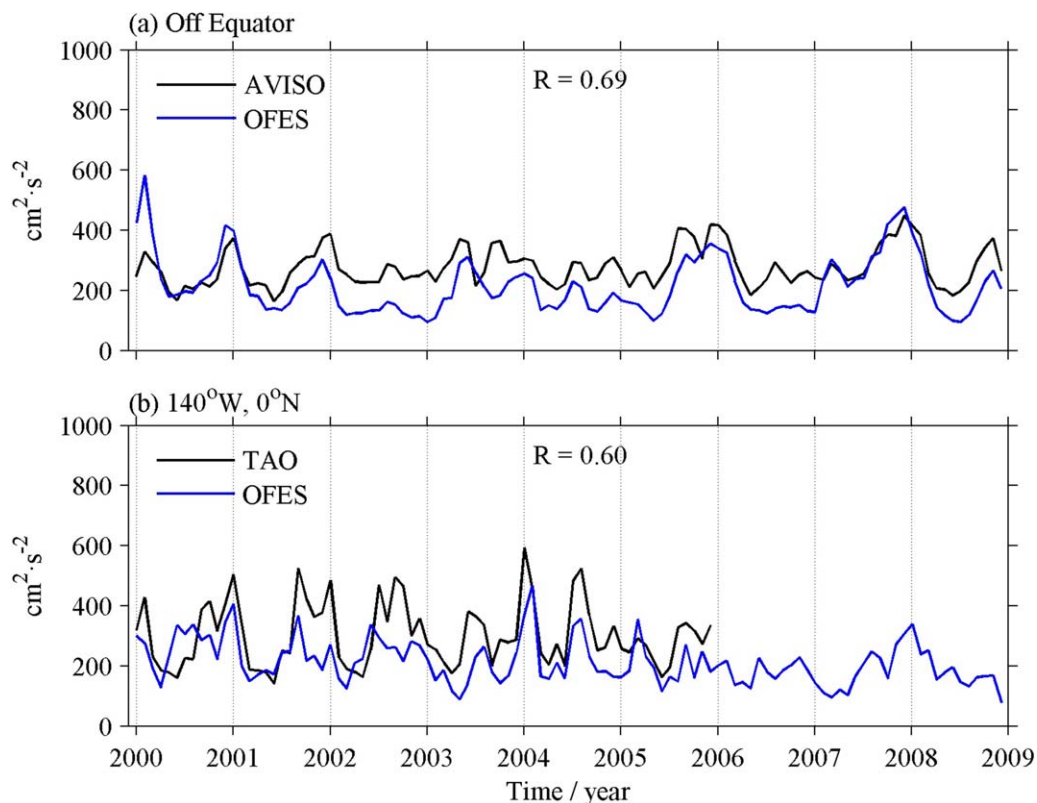


Figure 4. Monthly EKE time series in the year 2000–2008: (a) Off Equator, averaged in the black box of Figure 2 calculated from the SLA data of AVISO (black line) and OFES (blue line); (b) at 140°W, 0°N, averaged in the upper 100 m calculated from the horizontal velocity data of TAO (black line) and OFES (blue line). Their linear correlation coefficients reach (a) 0.69 and (b) 0.60, both of which pass the Student's *t* test 95% confidence level.

features and their linear correlation coefficient reaches 0.60, exceeding the Student's *t* test 95% confidence level (Figure 4b).

These favorable model-observation comparisons discussed above suggest that the OFES QSCAT-run data can capture well the spatial distribution and temporal variability of the observed EKE in the central and eastern equatorial Pacific Ocean that is indicative of the activity of TIWs. In addition, the OFES EKE is weaker than the observations by 22% in average (weaker 21% than AVISO and 23% than TAO, Figure 4), implying there is still room for improvement of the OGCM.

2.3. Method

The EKE in the TIWs scale, defined as the kinetic energy of the 60 days high-pass filtered horizontal velocity, can be converted from MKE and EPE via the barotropic and baroclinic instabilities, respectively. Following *Qiao and Weisberg* [1998], the barotropic eddy energy conversion rate (BTR) and baroclinic eddy energy conversion rate (BCR) are estimated by

$$BTR = -\langle u'u' \rangle U_x - \langle u'v' \rangle (U_y + V_x) - \langle v'v' \rangle V_y, \quad (4)$$

$$BCR = \frac{-g\langle \rho'w' \rangle}{\rho_0}, \quad (5)$$

where (*u, v, w*) are velocity components in the conventional Cartesian coordinate system, angle brackets (or capital letters) denote 60 days averages as running means, primes denote deviations of individual variables about their running means, and subscripted variables denote partial differentiation. The density ρ in equation (5) is calculated from the potential temperature (*T*) and salinity (*S*) of OFES. The constant $\rho_0 = 1025 \text{ kg} \cdot \text{m}^{-3}$. In equation (4), BTR is calculated from the product of horizontal Reynolds momentum fluxes and horizontal shear of the mean flows. It represents the kinetic energy conversion between MKE and EKE by eddy diffusion processes [*McWilliams*, 2006]. In equation (5), BCR is calculated from the vertical Reynolds density fluxes. It represents the energy conversion between EPE and EKE [*Johnson*, 1996]. Positive (negative) values of BTR or BCR act to increase (decrease) the EKE.

3. Mechanism of the Seasonal EKE Variability

The barotropic and baroclinic instabilities were proved to be the energy source for EKE in the TIWs area by early studies [*Philander*, 1978; *Cox*, 1980; *Weisberg*, 1984; *Luther and Johnson*, 1990]. We will revisit eddy energetics over the region and discuss the seasonal variability of EKE, BTR, and BCR as well as the dynamic processes governing the seasonal variability of EKE using the OFES simulations.

3.1. Seasonal Variability of EKE, BTR, and BCR

In the annual mean state, the elevated EKE signal is located in the region of 0°N–6°N, 180°W–100°W (the black box in Figure 5a) and is mostly confined to the upper ocean above the thermocline as represented by the 20°C isotherm (Figures 5b and 5c). This spatial pattern of EKE agrees well with the result calculated from the Lagrangian surface drifters [*Zheng et al.*, 2016, Figure 1d]. Similar to EKE, large BTR and BCR values are mostly located at 0°N–6°N in the upper 100 m, above the thermocline (Figure 6). Averaged in the upper 100 m, the spatial patterns of BTR and BCR are consistent with the distribution of high EKE (Figure 7). In more details, high positive BTR is distributed zonally into two bands of 0°N–2°N and 2°N–6°N, respectively (Figure 7a). The equatorial band represents the horizontal shear instability between the EUC and SEC, while the north band represents the horizontal shear instability between the SEC and NECC. Positive BCR represents that the potential energy is converted from EPE to EKE at the meridional front between the equatorial upwelling and the SEC flank north of the equator. The results in Figure 7 confirm that the barotropic and baroclinic instabilities are both the energy sources for EKE in the TIWs area of the annual mean state [*Philander*, 1978; *Cox*, 1980; *Weisberg*, 1984; *Luther and Johnson*, 1990].

Averaged between 0°N and 6°N, the seasonal EKE, BTR, and BCR anomalies exhibit very similar seasonal cycles (Figure 8). The positive anomalies propagate westward from 100°W in June to 180°W in December, with phase shift at about $-0.57 \text{ m} \cdot \text{s}^{-1}$ close to the theoretical phase speed of long baroclinic Rossby waves in the region [*Chelton and Schlax*, 1996]. The contributions of the BTR ($2.04 \times 10^{-4} \text{ cm}^2 \text{ s}^{-3}$) and BCR ($2.30 \times 10^{-4} \text{ cm}^2 \text{ s}^{-3}$) to the seasonal EKE are almost equal (Table 1). Therefore, it is found that the seasonal

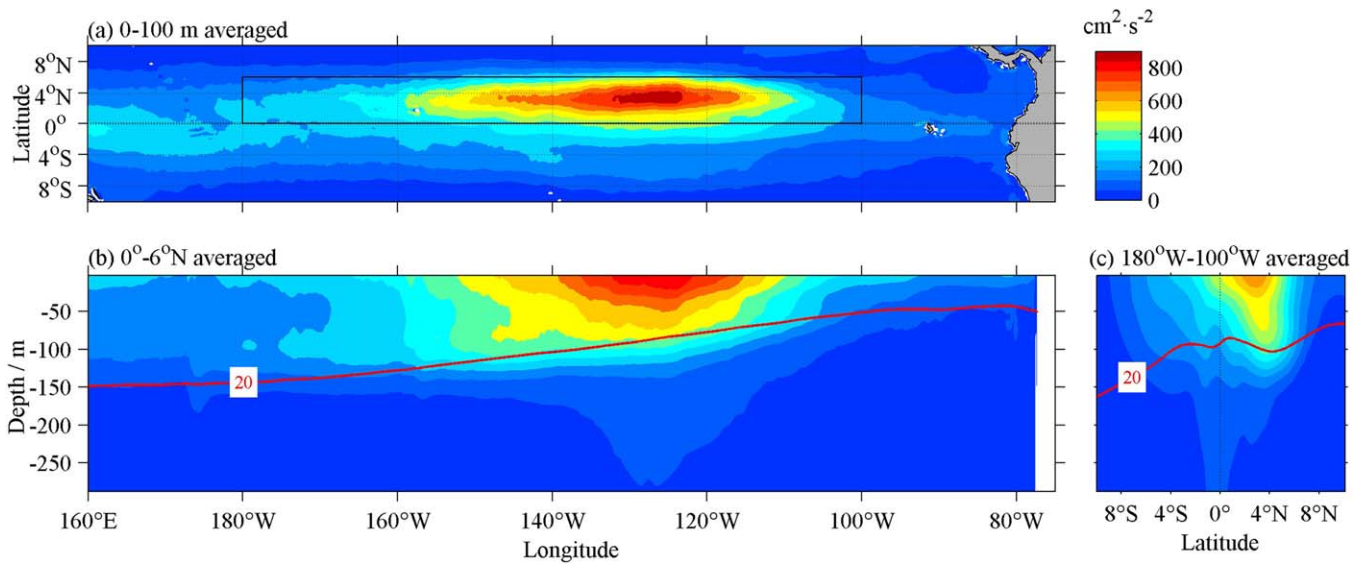


Figure 5. Spatial distributions of the annual mean EKE calculated from velocities of OFES averaged (a) in the upper 100 m, (b) between 0°N and 6°N, and (c) between 180°W–100°W. Box (0°N–6°N, 180°W–100°W) in (a) represents the region of elevated EKE related to the TIWs. Red lines in Figures 5b and 5c represent the annual mean 20°C isotherm.

variability of EKE, governed by the seasonal variability of the barotropically-baroclinically unstable upper ocean circulation, is featured with a westward propagation at the phase speed of long baroclinic Rossby waves.

3.2. Dynamic Processes Governing the Seasonal Variability of BTR and BCR

With the barotropically-baroclinically unstable upper ocean circulation, TIWs develop in the central and eastern Pacific Ocean. In order to clarify the dynamic processes governing the seasonal variability of BTR and BCR, each term in BTR and BCR is examined (Table 1). As expected, the $-\langle u'v' \rangle U_y$ is the dominant term of BTR because of the predominantly zonal circulation in the region [Kessler, 2006]. Extremely large positive BTR is mostly located in the shear-region of the SEC and NECC, which are in thermal-wind balance with the thermocline trough along 4°N (Figure 6a). Large positive BCR is located in the south slope of the thermocline trough due to the large meridional temperature gradient there (Figure 6b) and this explains why the

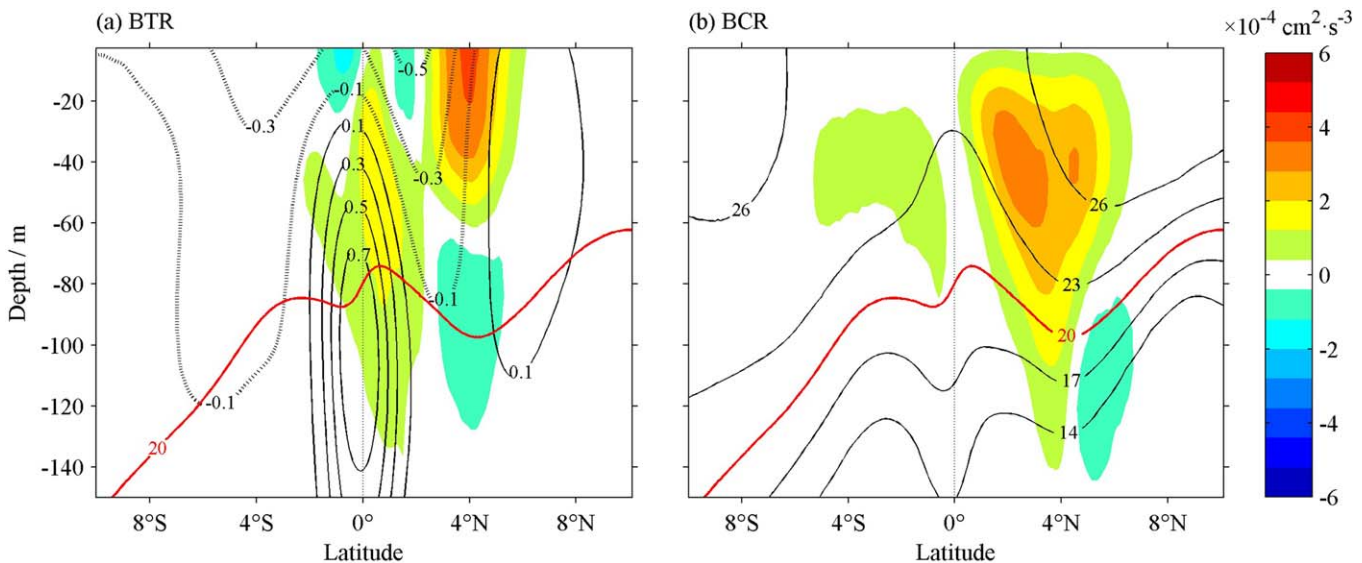


Figure 6. Meridional sections of the annual mean: (a) BTR (shading) and zonal current (black contour, unit: $m \cdot s^{-1}$); (b) BCR (shading) and the isotherms (black contour) averaged between 180°W–100°W. The red contours in Figures 6a and 6b represent the 20°C isotherm.

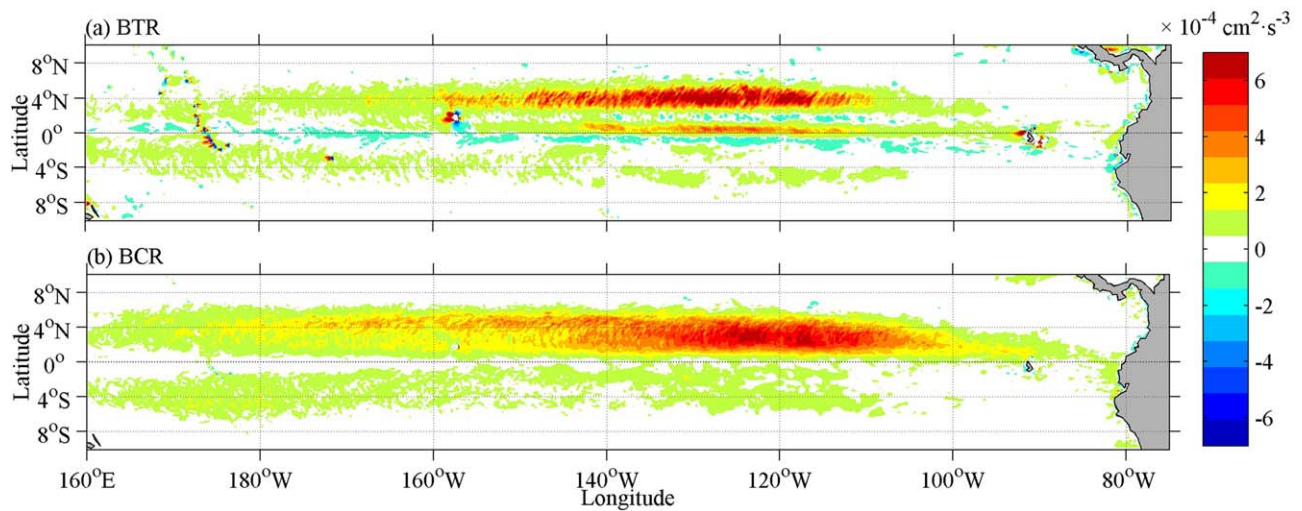


Figure 7. Annual mean (a) BTR and (b) BCR averaged in the upper 100 m calculated from OFES. See equations (5) and (6) for the formulas of BTR and BCR.

most elevated EKE exists in the south of 4°N (Figure 5c). As the BTR and BCR are both related to the ocean stratification, the spatial structure of the thermocline is taken into account [Kessler, 2006]. The BTR is linked to the ocean stratification by the thermal-wind balance.

$$\langle u'v' \rangle = -v_e U_y, \tag{6}$$

$$BTR \approx -\langle u'v' \rangle U_y = v_e U_y^2, \tag{7}$$

$$U = -\frac{g\alpha}{f} \int_{z_0}^z \frac{\partial \bar{T}}{\partial y} dz, \tag{8}$$

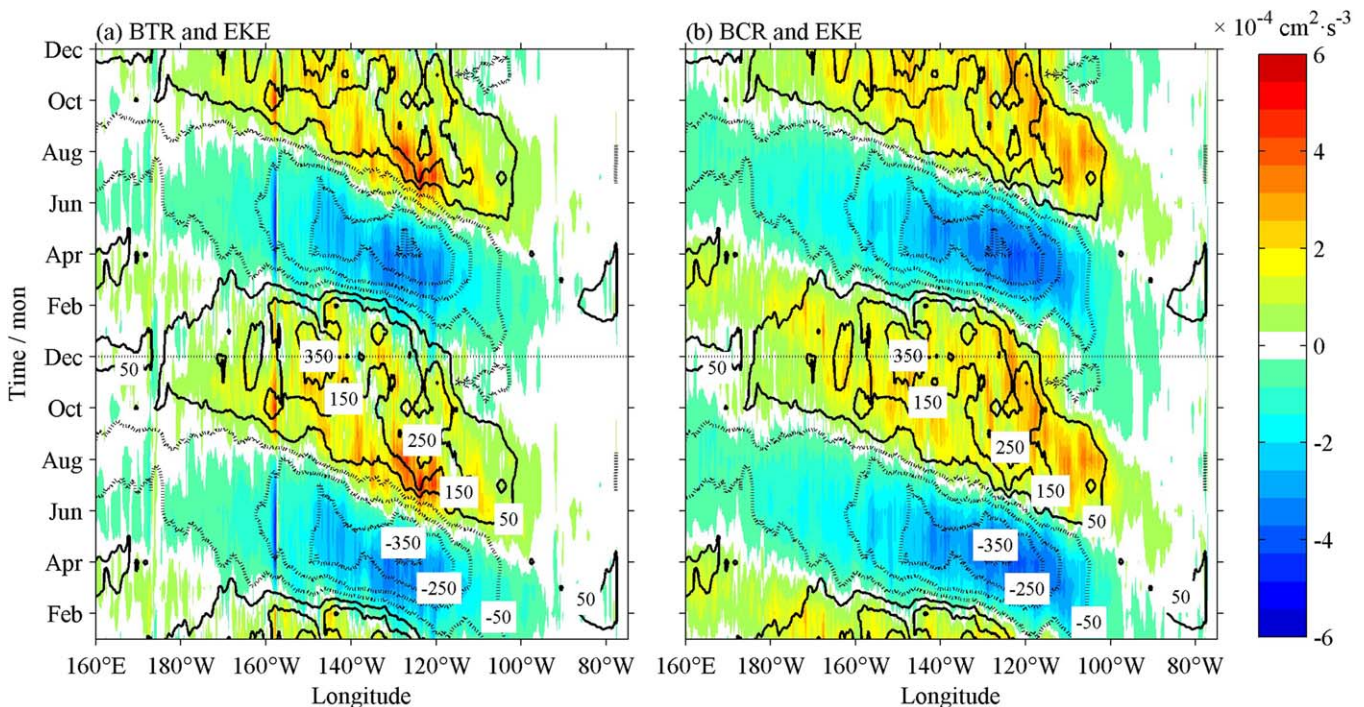


Figure 8. Seasonal anomalies of (a) BTR (shading) and EKE (contour, unit: $\text{cm}^2 \cdot \text{s}^{-2}$), (b) BCR (shading) and EKE (contour) averaged between 0°N–6°N.

Table 1. Each Terms of the BTR and BCR Averaged in the Box of Figure 5a

BTR, Unit: $\times 10^{-4} \text{cm}^2 \cdot \text{s}^{-3}$				BCR, Unit: $\times 10^{-4} \text{cm}^2 \cdot \text{s}^{-3}$
$-(u'u')U_x$	$-(u'v')U_y$	$-(u'v')V_x$	$-(v'v')V_y$	$-\frac{g(\rho'w')}{\rho_0}$
0.01	2.14	-0.01	-0.10	2.30

$$BTR \approx -\frac{\nu_e g^2 \alpha^2}{f^2} \left\{ \int_{z_0}^z \frac{\partial^2 \bar{T}}{\partial y^2} dz \right\}^2 \quad (9)$$

Equation (6) is the parameterization of the eddy-mean flow interaction, where ν_e is the eddy viscosity coefficient [McWilliams, 2006], with an estimation of $\sim 2 \times 10^4 \text{ m}^2 \cdot \text{s}^{-1}$ in the central and eastern equatorial Pacific [Zhurbas and Oh, 2004]. From equation (7) the BTR is simply related to the meridional shear of the zonal currents. Equation (8) is the thermal-wind balance, where $\alpha = \frac{\Delta \rho}{\rho_0} = 0.003$, and \bar{T} is the monthly potential temperature. It can be seen that the BTR is related to the thermocline troughs or ridges $\frac{\partial^2 \bar{T}}{\partial y^2}$ as in equation (9). Simultaneously, the BCR is related to the thermocline trough because the meridional ocean temperature gradient is sharper when the thermocline trough is deeper along 4°N.

In the annual mean state, the northern equatorial part of the SEC flows westward at 1°N–4°N, while the NECC flows eastward at 4°N–8°N (Figure 9a). The thermocline depth is simply defined as the depth of 20°C isotherm (D_{20}). The SEC and NECC are trapped above the southern and northern slopes of the thermocline trough in thermal-wind balance, respectively. Large positive BTR exists above the zonal thermocline trough along 4°N. Here we define the seasonal BTR index as the 12 months high-pass filtered monthly BTR values averaged between 180°W and 100°W along 4°N in 2000–2008. It represents the seasonal variability of BTR. A linear regression of the thermocline depth and horizontal currents to the seasonal BTR index shows that the seasonal variability of BTR is closely related to the thermocline along 4°N and the trapped zonal currents (Figure 9b). The meridional shear of the zonal currents and thus the BTR are reinforced when the thermocline trough gets deeper along 4°N in thermal-wind balance with the stronger SEC and NECC. The relationship between the thermocline and the BTR and BCR is further examined (Figure 10). The seasonal BTR anomaly moves westward along with the thermocline trough anomaly along 4°N. The BCR anomaly shows the same westward movement as the BTR (figure not shown). The positive BTR and BCR anomalies move

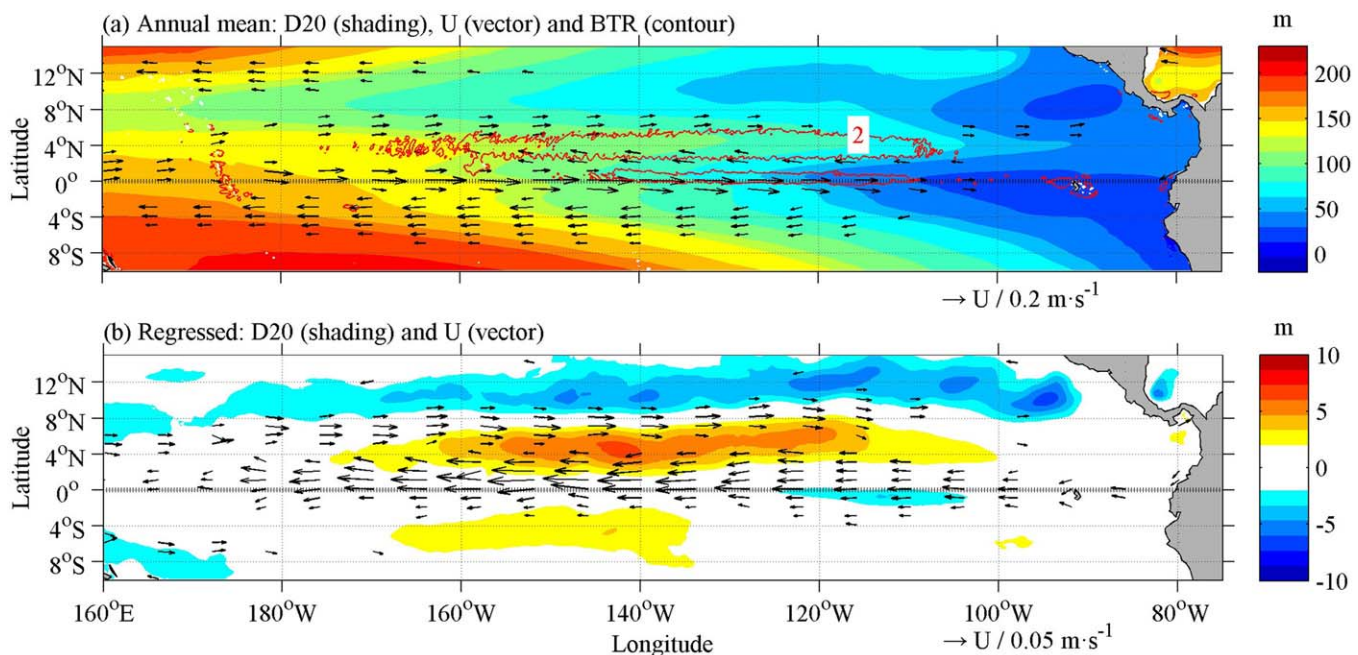


Figure 9. Horizontal distributions of (a) annual mean D_{20} (shading), horizontal currents (vector) averaged above the annual mean D_{20} and BTR (contour, unit: $\times 10^{-4} \text{cm}^2 \cdot \text{s}^{-3}$); (b) linear regressions of D_{20} (shading) and horizontal currents (vector) to the 12 months high-pass filtered BTR averaged between 180°W–100°W along 4°N.

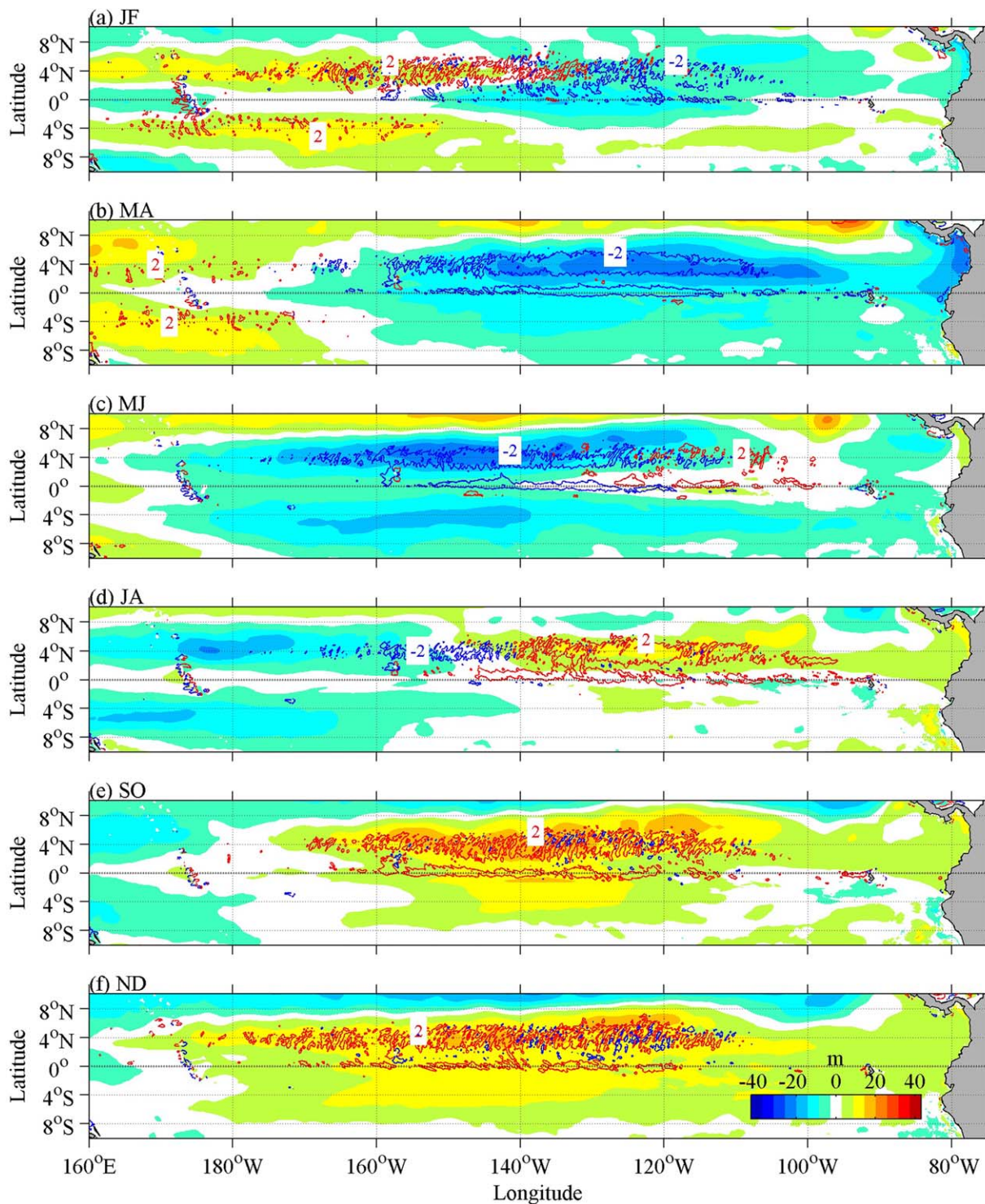


Figure 10. Bi-monthly anomalies of D_{20} (shading) and BTR (contour, unit: $\times 10^{-4} \text{ cm}^2 \cdot \text{s}^{-3}$): (a) January and February, (b) March and April, (c) May and June, (d) July and August, (e) September and October, and (f) November and December.

westward from 100°W in June to 180°W in December, along with the westward propagation of the thermocline trough anomalies. In conclusion, the seasonal EKE anomaly moving westward is governed by the westward propagation of the thermocline trough anomalies along 4°N in thermal-wind balance with the seasonal variability of the barotropically-baroclinically unstable upper ocean circulation (Figure 11).

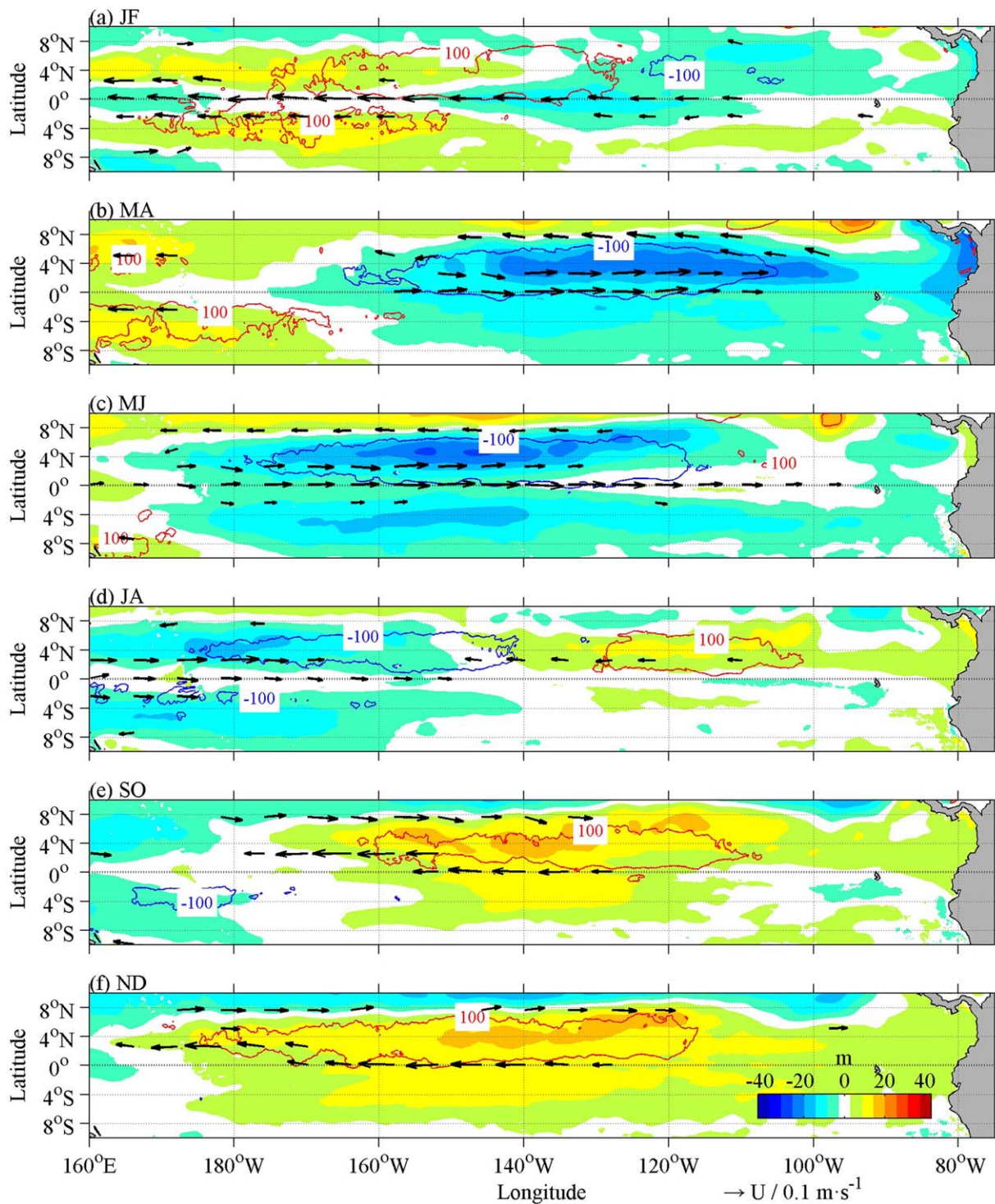


Figure 11. Bi-monthly anomalies of D_{20} (shading), horizontal currents (vector), and EKE (contour, unit: $\text{cm}^2 \cdot \text{s}^{-2}$): (a) January and February, (b) March and April, (c) May and June, (d) July and August, (e) September and October, and (f) November and December.

4. Discussion

In the present study, the westward expansion of the EKE from 100°W in June to 180°W in December has been shown to be governed by the westward propagation of the seasonal-varying thermocline trough along 4°N . In order to explore the cause underlying the seasonal variability of the thermocline trough, the

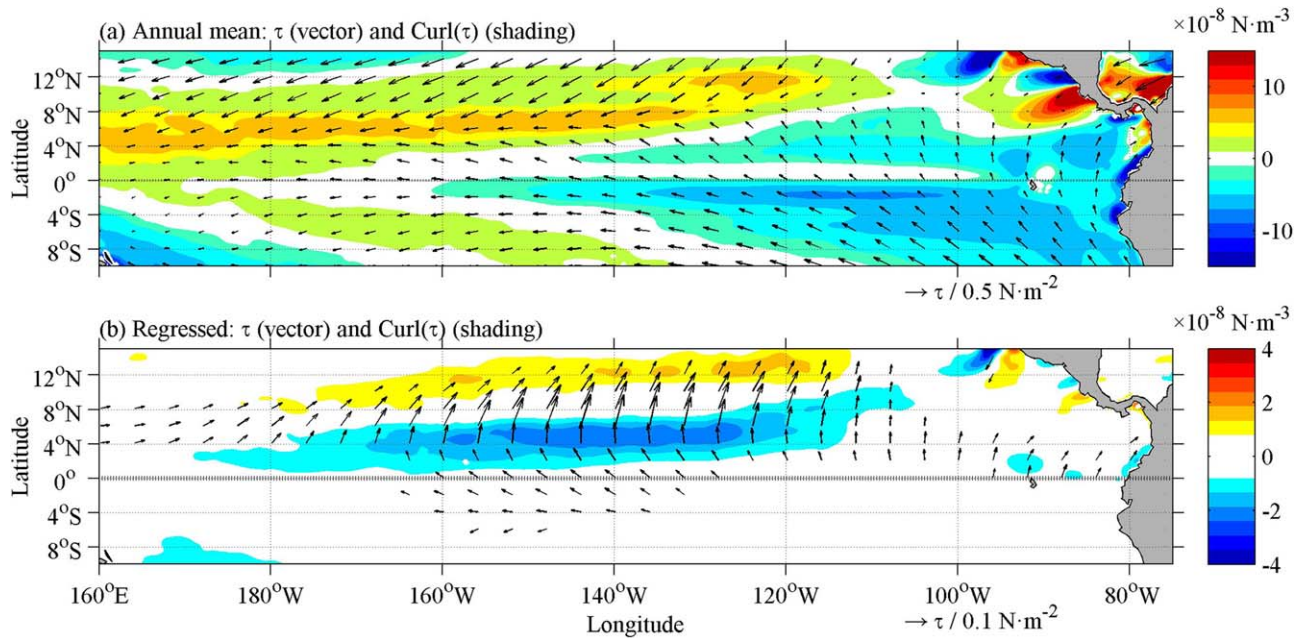


Figure 12. Horizontal distributions of (a) annual mean surface wind stresses (vector) and wind stress curls (shading); (b) linear regressions of the surface wind stresses (vector) and wind stress curls (shading) to the 12 months high-pass filtered D_{20} averaged between 180°W and 100°W along 4°N .

surface wind stresses are analyzed. In the annual mean state, there exists a weak cross-equatorial component of trade winds in the east of 160°W along 4°N (Figure 12a). The effect of the trade winds on the thermocline is examined by a linear regression to the seasonal D_{20} anomaly averaged between 180°W and 100°W along 4°N . It can be seen from Figure 12b that the D_{20} is deepened when there appear negative wind stress curls and southerly winds. This relationship is further confirmed using an $1\frac{1}{2}$ -layer reduced-gravity model along 4°N as follows [Qiu, 2002; Cheng *et al.*, 2016; Chen *et al.*, 2016]. The linear vorticity equation governing the D_{20} anomaly $H(x, t)$ in the $1\frac{1}{2}$ -layer reduced-gravity model is given under the longwave approximation by

$$\frac{\partial H}{\partial t} - C_R \frac{\partial H}{\partial x} = -\nabla \times \left(\frac{\bar{\tau}}{\rho_0 f} \right) - \varepsilon H, \quad (10)$$

where C_R is the phase speed of long baroclinic Rossby waves, $C_R = -\frac{\beta g' \overline{D_{20}}}{f^2}$, β is the meridional gradient of the Coriolis parameter f , g' is the reduced gravity, $g' = ag$, and $\overline{D_{20}}$ is the annual mean D_{20} . The value of C_R is much dependent on latitude ϕ through f and $\nabla \times$ represents the vertical component of the curl vector. $\bar{\tau}$ is the surface wind stress anomaly vector from the output of the OFES QSCAT-run and ε is the Newtonian dissipation rate, whose reciprocal is the e -folding time. When integrated from the eastern boundary (x_e) along the characteristic of the long baroclinic Rossby waves, the solution of equation (10) can be solved by

$$H(x, t) = H \left(x_e, t + \frac{x - x_e}{C_R} \right) \exp \left[\varepsilon \frac{(x - x_e)}{C_R} \right] + \frac{1}{C_R} \int_{x_e}^x \nabla \times \left[\frac{\bar{\tau} \left(x', t + \frac{x - x'}{C_R} \right)}{\rho_0 f} \right] \exp \left[\varepsilon \frac{(x - x')}{C_R} \right] dx' \quad (11)$$

The first term on the right-hand side of equation (11) represents the influence of the thermocline signals propagating from the eastern boundary x_e . In this study, the eastern-boundary thermocline depth is set as the D_{20} derived from the OFES QSCAT-run. The second term represents the thermocline response due to the interior wind stress forcing. For the case along 4°N , the relevant parameters are set as below $\overline{D_{20}} = 80\text{m}$, $g' = 0.003g$, $C_R = -0.52\text{m} \cdot \text{s}^{-1}$, $\varepsilon = (2\text{months})^{-1}$.

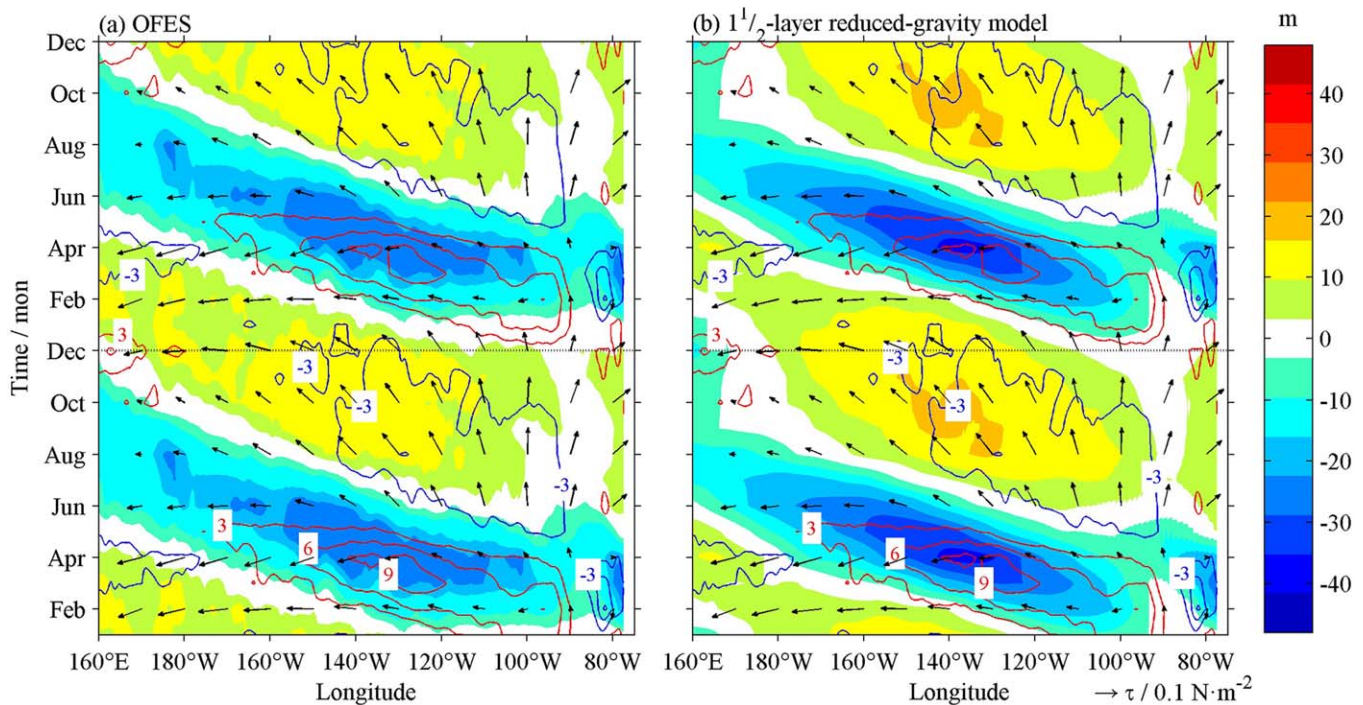


Figure 13. Seasonal evolutions of the surface wind stress anomalies (vector), the Ekman pumping velocity anomalies (contour, unit: $\times 10^{-6} \text{ m} \cdot \text{s}^{-1}$) and D_{20} anomalies (shading) along 4°N from the output of (a) OFES QSCAT-run and (b) an $1\frac{1}{2}$ -layer reduced-gravity model forced by the surface wind stresses.

Compared with the seasonal cycle of the D_{20} anomaly along 4°N from the OFES QSCAT-run, the result of the $1\frac{1}{2}$ -layer reduced-gravity model is very favorable (Figure 13). In both models, the thermocline is forced by an anticyclonic wind stress anomaly when the southerly winds develop from June to December. The thermocline trough deepens from June to December. Strong forcing of the surface wind stresses mostly exists between 160°W and 90°W . The thermocline anomalies are accumulated between 180°W and 100°W by the westward propagation of the thermocline response with the e -folding distance of 24° of longitude along 4°N . This further verifies that the seasonal variability of the thermocline trough is forced by the seasonal-varying surface wind stresses, which accounts for the high seasonal EKE anomalies between 180°W and 100°W (Figure 8).

5. Summary

Based on the observations and high-resolution OGCM outputs, elevated EKE signal exists along 4°N between 180°W and 100°W in the eastern equatorial Pacific, above the main thermocline trough. This EKE exhibits a significant annual cycle with the positive anomalies moving westward from 100°W in June to 180°W in December. This seasonal variability of EKE is related to the mixed barotropic-baroclinic instabilities, and the contributions of them are almost equal, which modulates seasonally as governed by seasonal perturbations of the thermocline trough at 4°N . As the thermocline trough becomes deeper, its associated zonal currents become barotropically-baroclinically more unstable. The seasonal perturbations of the thermocline trough are linked to the forcing of the surface wind stresses. The thermocline trough is deepened by the accumulation of surface wind stress forcing when the seasonal-dependent southerly winds develop from June to December. It is worth emphasizing that the seasonal-varying EKE is related to the barotropically-baroclinically unstable upper ocean circulation that is modulated by the thermocline trough and the southerly winds along 4°N .

Eddies in the central and eastern equatorial Pacific Ocean can potentially couple with the surface wind stresses [Chelton *et al.*, 2001], affecting the regional mixing of water properties [Moum *et al.*, 2013; Liu *et al.*, 2016] and the heat budget of the cold tongue, which is a critical region to the development of El Niño and Southern Oscillation (ENSO) [Swenson and Hansen, 1999]. Further studies are needed to clarify the

relationship between the TIWs eddies and the surface wind stresses on the interannual time scales, and its impacts on the heat budget of the cold tongue and ultimately on the development of ENSO.

Acknowledgments

We would like to acknowledge Ruixin Huang from Woods Hole Oceanographic Institution for useful advices. The OFES simulation was conducted on the Earth Simulator under the support of JAMSTEC. The OFES QSCAT-run output used in our study is obtained from APDRC, University of Hawaii (<http://apdrc.soest.hawaii.edu>). The OISST (Optimum Interpolation Sea Surface Temperature) data are obtained from NOAA (<http://www.ncdc.noaa.gov/oisst>). The AVISO product is obtained from CNES (<http://www.aviso.altimetry.fr>). The TAO data are obtained from PMEL, NOAA (<http://www.pmel.noaa.gov/gtmba>). The Matrix Laboratory (MATLAB) Seawater toolbox was developed by Phil Morgan, CSIRO (<http://www.marine.csiro.au>). This study is supported by the National Natural Science Foundation of China (41525019, 41521005, 41522601, and 41676002), Strategic Priority Research Program of the Chinese Academy of Sciences (XDA11010000), the State Oceanic Administration of China (GASI-IPOVAI-02), and the CAS/SAFEA International Partnership Program for Creative Research Teams and the China Scholarship Council.

References

- Baturin, N., and P. Niiler (1997), Effects of instability waves in the mixed layer of the equatorial Pacific, *J. Geophys. Res.*, *102*(C13), 27,771–27,793.
- Bryden, H. L., and E. C. Brady (1989), Eddy momentum and heat fluxes and their effects on the circulation of the equatorial Pacific Ocean, *J. Mar. Res.*, *47*(1), 55–79.
- Chelton, D. B., and M. G. Schlax (1996), Global observations of oceanic Rossby waves, *Science*, *272*(5259), 234–238.
- Chelton, D. B., S. K. Esbensen, M. G. Schlax, N. Thum, M. H. Freilich, F. J. Wentz, C. L. Gentemann, M. J. McPhaden, and P. S. Schopf (2001), Observations of coupling between surface wind stress and sea surface temperature in the eastern tropical Pacific, *J. Clim.*, *14*(7), 1479–1498.
- Chen, X., B. Qiu, Y. Du, S. Chen, and Y. Qi (2016), Interannual and interdecadal variability of the North Equatorial Countercurrent in the western Pacific, *J. Geophys. Res. Oceans*, *121*, 7743–7758, doi:10.1002/2016JC012190.
- Cheng, X., S.-P. Xie, Y. Du, J. Wang, X. Chen, and J. Wang (2016), Interannual-to-decadal variability and trends of sea level in the South China Sea, *Clim. Dyn.*, *46*(9–10), 3113–3126.
- Cox, M. D. (1980), Generation and propagation of 30-day waves in a numerical-model of the Pacific, *J. Phys. Oceanogr.*, *10*(8), 1168–1186.
- Duing, W., P. Hisard, E. Katz, J. Meincke, L. Miller, K. V. Moroshkin, G. Philander, A. A. Ribnikov, K. Voigt, and R. Weisberg (1975), Meanders and long waves in equatorial Atlantic, *Nature*, *257*(5524), 280–284.
- Flament, P. J., S. C. Kennan, R. A. Knox, P. P. Niiler, and R. L. Bernstein (1996), The three-dimensional structure of an upper ocean vortex in the tropical Pacific Ocean, *Nature*, *383*(6601), 610–613.
- Hansen, D. V., and C. A. Paul (1984), Genesis and effects of long waves in the equatorial Pacific, *J. Geophys. Res.*, *89*(C6), 10,431–10,440.
- Hayes, S., L. Mangum, J. Picaut, A. Sumi, and K. Takeuchi (1991), TOGA-TAO: A moored array for real-time measurements in the tropical Pacific Ocean, *Bull. Am. Meteorol. Soc.*, *72*(3), 339–347.
- Jochum, M., and R. Murtugudde (2006), Temperature advection by tropical instability waves, *J. Phys. Oceanogr.*, *36*(4), 592–605.
- Johnson, E. S. (1996), A convergent instability wave front in the central tropical Pacific, *Deep Sea Res., Part II*, *43*(4), 753–778.
- Kessler, W. S. (2006), The circulation of the eastern tropical Pacific: A review, *Prog. Oceanogr.*, *69*(2), 181–217.
- Legeckis, R. (1977), Long waves in the eastern equatorial Pacific Ocean: A view from a geostationary satellite, *Science*, *197*(4309), 1179–1181.
- Liu, C. Y., A. Kohl, Z. Y. Liu, F. Wang, and D. Stammer (2016), Deep-reaching thermocline mixing in the equatorial Pacific cold tongue, *Nat. Commun.*, *7*, 11576, doi:10.1038/ncomms11576.
- Luther, D. S., and E. S. Johnson (1990), Eddy energetics in the upper equatorial Pacific during the Hawaii-to-Tahiti Shuttle Experiment, *J. Phys. Oceanogr.*, *20*(7), 913–944.
- Marchesiello, P., X. Capet, C. Menkes, and S. C. Kennan (2011), Submesoscale dynamics in tropical instability waves, *Ocean Model.*, *39*(1–2), 31–46.
- Masina, S., S. G. H. Philander, and A. B. G. Bush (1999), An analysis of tropical instability waves in a numerical model of the Pacific Ocean: 2. Generation and energetics of the waves, *J. Geophys. Res.*, *104*(C12), 29,637–29,661.
- Masumoto, Y., H. Sasai, T. Kagimoto, N. Komori, A. Ishida, Y. Sasai, T. Miyama, T. Motoi, H. Mitsudera, and K. Takahashi (2004), A fifty-year eddy-resolving simulation of the world ocean: Preliminary outcomes of OFES (OGCM for the Earth Simulator), *J. Earth Simul.*, *1*, 35–56.
- McWilliams, J. C. (2006), *Fundamentals of Geophysical Fluid Dynamics*, pp. 102–103, Cambridge Univ. Press, Cambridge, U. K.
- Moum, J. N., A. Perlin, J. D. Nash, and M. J. McPhaden (2013), Seasonal sea surface cooling in the equatorial Pacific cold tongue controlled by ocean mixing, *Nature*, *500*(7460), 64–67, doi:10.1038/nature12363.
- Pacanowski, R. C., and S. M. Griffies (2000), Mom 3.0 manual, technical report, 680 pp., Geophys. Fluid Dyn. Lab., Princeton, N. J.
- Philander, S. (1976), Instabilities of zonal equatorial currents, *J. Geophys. Res.*, *81*(21), 3725–3735.
- Philander, S. G. H. (1978), Instabilities of zonal equatorial currents, 2, *J. Geophys. Res.*, *83*(C7), 3679–3682.
- Qiao, L., and R. H. Weisberg (1995), Tropical instability wave kinematics: Observations from the tropical instability wave experiment, *J. Geophys. Res.*, *100*(C5), 8677–8693.
- Qiao, L., and R. H. Weisberg (1998), Tropical instability wave energetics: Observations from the tropical instability wave experiment, *J. Phys. Oceanogr.*, *28*(2), 345–360.
- Qiu, B. (1999), Seasonal eddy field modulation of the north Pacific subtropical countercurrent: TOPEX/Poseidon observations and theory, *J. Phys. Oceanogr.*, *29*(10), 2471–2486.
- Qiu, B. (2002), Large-scale variability in the midlatitude subtropical and subpolar north Pacific Ocean: Observations and causes, *J. Phys. Oceanogr.*, *32*(1), 353–375.
- Sasaki, H., Y. Sasai, S. Kawahara, M. Furuichi, F. Araki, A. Ishida, Y. Yamanaka, Y. Masumoto, and H. Sakuma (2004), A series of eddy-resolving ocean simulations in the world ocean: OFES (OGCM for the Earth Simulator) project, vol. 3, pp. 1535–1541, IEEE TECHNO-OCEAN'04, N. J.
- Sasaki, H., M. Nonaka, Y. Masumoto, Y. Sasai, H. Uehara, and H. Sakuma (2008), An eddy-resolving hindcast simulation of the quasiglobal ocean from 1950 to 2003 on the Earth Simulator, in *High Resolution Numerical Modelling of the Atmosphere and Ocean*, edited by K. Hamilton and W. Ohfuchi, pp. 157–185, Springer, New York.
- Swenson, M. S., and D. V. Hansen (1999), Tropical Pacific Ocean mixed layer heat budget: The Pacific cold tongue, *J. Phys. Oceanogr.*, *29*(1), 69–81.
- Wang, W., and M. J. McPhaden (1999), The surface-layer heat balance in the equatorial Pacific Ocean. Part I: Mean seasonal cycle, *J. Phys. Oceanogr.*, *29*(8), 1812–1831.
- Weisberg, R. H. (1984), Instability waves observed on the equator in the Atlantic-Ocean during 1983, *Geophys. Res. Lett.*, *11*(8), 753–756.
- Zheng, S., M. Feng, Y. Du, X. Cheng, and J. Li (2016), Annual and interannual variability of the tropical instability vortices in the equatorial eastern Pacific observed from Lagrangian surface drifters, *J. Clim.*, *29*(24), 9163–9177.
- Zhurbas, V., and I. S. Oh (2004), Drifter-derived maps of lateral diffusivity in the Pacific and Atlantic oceans in relation to surface circulation patterns, *J. Geophys. Res.*, *109*, C05015, doi:10.1029/2003JC002241.